








β -decay feeding intensity distribution of ^{64}Mn

W. W. von Seeger ^{1,*} P. A. DeYoung ¹ A. Spyrou,^{2,3,4} S. Karampagia ^{3,5} E. F. Brown ^{2,3,4,6} S. Ahn,^{4,7,8} B. P. Crider,⁹ A. C. Dombos,^{2,3,4} G. W. Hitt ¹⁰ C. Langer,¹¹ R. Lewis,^{3,12} S. N. Liddick,^{3,12} S. Lyons ^{3,4} Z. Meisel,^{4,13} F. Montes,^{3,4} F. Naqvi,^{3,14} W.-J. Ong,^{2,3,15} C. F. Persch ¹ J. Pereira,^{3,4} H. Schatz,^{2,3,4} and K. Schmidt^{3,4,16}

¹*Department of Physics, Hope College, Holland, Michigan 49423, USA*

²*Department of Physics and Astronomy, Michigan State University, East Lansing, Michigan 48824, USA*

³*Facility for Rare Isotope Beams, Michigan State University, East Lansing, Michigan 48824, USA*

⁴*Joint Institute for Nuclear Astrophysics—Center for the Evolution of the Elements, Michigan State University, East Lansing, Michigan 48824, USA*

⁵*Grand Valley State University, Allendale, Michigan 49401, USA*

⁶*Department of Computational Mathematics, Science, and Engineering, Michigan State University, East Lansing, Michigan 48824, USA*

⁷*Cyclotron Institute, Texas A&M University, College Station, Texas 77843, USA*

⁸*Center for Exotic Nuclear Studies, Institute for Basic Science, Daejeon 34126, South Korea*

⁹*Department of Physics and Astronomy, Mississippi State University, Mississippi State, Mississippi 39762, USA*

¹⁰*Department of Physics and Engineering Science, Coastal Carolina University, Conway, South Carolina 29528, USA*

¹¹*University of Applied Sciences Aachen, 52066 Aachen, Germany*

¹²*Department of Chemistry, Michigan State University, East Lansing, Michigan 48824, USA*

¹³*Department of Physics and Astronomy, Ohio University, Athens, Ohio 45701, USA*

¹⁴*Department of Nuclear Engineering, Texas A&M University, College Station, Texas 77840, USA*

¹⁵*Nuclear and Chemical Sciences Division, Lawrence Livermore National Laboratory, Livermore, California 94550, USA*

¹⁶*Institute of Radiation Physics, Helmholtz-Zentrum Dresden-Rossendorf, Bautzner Landstrasse 400, 01328 Dresden, Germany*



(Received 9 May 2023; revised 19 February 2024; accepted 20 March 2024; published 5 April 2024)

Nuclei around the $N = 40$ “island of inversion” exhibit interesting structure features that have been the focus of several experimental and theoretical studies. The present work presents the first complete study of the β -decay feeding intensity distribution and Gamow-Teller distribution for the β decay of ^{64}Mn to ^{64}Fe up to ≈ 10 MeV. The β -decay intensity function was extracted from total absorption spectroscopy measurements made at the National Superconducting Cyclotron Laboratory with the Summing NaI(Tl) (SuN) detector. The experimental results are compared to shell model calculations with and without the inclusion of the $\nu g_{9/2}$ orbital. From this comparison it is clear that the $\nu g_{9/2}$ orbital is essential for the accurate description of the ^{64}Fe β -decay strength above ≈ 3 MeV, emphasizing once again the transitional nature of this nucleus into the $N = 40$ island of inversion.

DOI: [10.1103/PhysRevC.109.044312](https://doi.org/10.1103/PhysRevC.109.044312)

I. INTRODUCTION

During the last two decades significant effort has been devoted towards the understanding of the nuclear structure in exotic nuclei, i.e. nuclei with extreme neutron to proton ratios. In particular, on the neutron-rich side of the valley of stability, traditional closed shells have been observed to break down in regions that are now known as “islands of inversion” [1]. Around the $N = 40$ island of inversion [2–4], isotopes of Fe and Cr were observed to exhibit increased collectivity with increasing number of neutrons towards $N = 40$. This was attributed to strong quadrupole correlations, which cause the

spherical configurations around the $N = 40$ subshell closure to compete energetically with the deformed “intruder” configurations. This competition can even appear in the ground states of the involved isotopes. In the present work we focus on the study of ^{64}Fe , which is considered to be at the transition of the Fe isotopic chain into the $N = 40$ island of inversion.

^{64}Fe has been the target of many experimental and theoretical studies. The β decay from ^{64}Mn populated low-spin discrete states in ^{64}Fe up to 4 MeV [5,6], since ^{64}Mn has a ground state spin-parity of 1^+ [7]. Higher spins were populated in two experiments using the $^{64}\text{Ni} + ^{238}\text{U}$ reaction [8,9] up to spin-parity of (10^+) and extending also up to 4 MeV of excitation energy. In addition to level-scheme information, 2^+ state lifetimes and $B(E2)$ values were reported in a multinucleon transfer experiment [10] and later confirmed

*wvonseeg@nd.edu

in a Coulomb excitation experiment [11]. Each of these experimental studies was compared to theoretical calculations, typically within the shell model. While in early studies the calculations were limited in the νfp model space, e.g., [8], it was clear that this was not enough to accurately describe ^{64}Fe and other nuclei in the region, except perhaps for the energy of the first 2^+ state [12]. During the last decade, large-scale shell model calculations, which include the $g_{9/2}$ and even the $d_{5/2}$ orbitals, have become possible, and those can typically reproduce the experimental results with high accuracy [2,9–11]. Nevertheless, all previous studies focused on the properties of the discrete level scheme at relatively low excitation energies. In the present work we present for the first time the full population of ^{64}Fe from the decay of ^{64}Mn , all the way to excitation energies of ≈ 10 MeV. The experimental results are compared with shell model calculations in the pf and $pf g$ model spaces, showing the importance of the inclusion of the $\nu g_{9/2}$ orbital in describing the β decay of ^{64}Mn .

Experimentally, the study of ^{64}Fe up to such high excitation energies is only possible through the use of the technique of total absorption spectroscopy (TAS) [13]. The power of the TAS method is that it uses large-volume γ -ray calorimeters to collect the energy from all emitted γ rays in a γ cascade. In this way, it is possible to identify the excitation energy populated during a β decay, without suffering from the ‘‘Pandemonium effect’’ [14]. Through these measurements, the β -decay intensity, I_β , and β -decay strength, $B(\text{GT})$, distributions can be extracted and compared to theoretical calculations. Several TAS detectors have been developed over the years, such as MTAS [15], SuN [16], and HECTOR [17,18] in the USA, and Lucrecia [19] and DTAS [20] in Europe. These devices have been used with diverse scientific goals, such as nuclear astrophysics [21–24], nuclear structure [25,26], and reactor applications [27–29]. Here we use the Summing NaI(Tl) (SuN) detector which was developed at Michigan State University, to study the structure of ^{64}Fe and explore further the region of rapid structure changes around the $N = 40$ island of inversion.

In addition to the nuclear structure impact, it is important to also note the astrophysical implications of the present work. Astrophysical calculations, especially for processes that extend far from stability, such as the r process [30] or processes in accreting neutron star crusts [31], often use nuclear theory to provide β -decay properties. It is therefore critical to compare the predictions of the theoretical calculations to experimental data, where available. Often these comparisons are done using integral quantities, such as the β -decay half-life, $T_{1/2}$, and β -delayed neutron emission probability, P_n [32–34]. It is beneficial, however, to compare these calculations to the full β -decay distributions, I_β and $B(\text{GT})$, since these are sensitive to nuclear structure effects that may be missed otherwise. Some astrophysical applications, such as accreting neutron star crust processes [31] or the r process in neutron star mergers [35,36] require reliable data for individual decay transition strengths.

Experimental details of beam production and delivery, the SuN detector, and active implantation target are given in Sec. II. Section III details particle identification, correlation of events, TAS analysis, and extraction of I_β and subsequent

calculation of $B(\text{GT})$. Section IV presents the experimental extracted I_β and $B(\text{GT})$, comparisons with shell model calculations, and a discussion of the shell model calculations. Finally, this work is summarized in Sec. V.

II. EXPERIMENTAL DETAILS

A primary beam of ^{82}Se at 140 MeV/u was created at the National Superconducting Cyclotron Laboratory (NSCL) at Michigan State University. The primary beam impinged on a Be target, producing a cocktail secondary beam containing ^{64}Mn . The secondary beam was then purified in the A1900 fragment separator [37,38]. On the way to the experimental end station, the secondary beam passed through an upstream thin timing scintillator and two silicon PIN detectors to measure the differential deposited energy ΔE and the time of flight for the identification of the implanted isotopes on an event-by-event basis. At the experimental end station the secondary beam was implanted in a 2 cm by 2 cm, 1 mm thick, 16×16 Double-Sided silicon-Strip Detector (DSSD). The DSSD was positioned in the center of the SuN detector [16]. The SuN detector is a 16 in. by 16 in. cylindrical 4π scintillation detector with a 1.8 in. diameter borehole through the center. The detector is separated into a top and bottom half, each of which consists of four optically isolated NaI(Tl) crystals each connected to three photomultiplier tubes. SuN has an average resolution of 6.1(2)% in each segment and an 85(2)% summing efficiency for the 662 keV photopeak of a ^{137}Cs source [16]. Signals from the DSSD were routed through a dual (high and low) gain preamplifier. This allowed the DSSD to detect the implantation of secondary beam particles (low-gain signal) and their subsequent β decays (high-gain signal). SuN detected the corresponding γ rays and β particles with sufficient energy to enter the active volume. A silicon surface barrier detector behind the DSSD functioned as a light-particle veto detector. More details about the setup can be found in Refs. [21,39,40].

III. ANALYSIS

A. Particle identification

The A1900 fragment separator was optimized for acceptance of ^{61}V [41] and produced a cocktail beam consisting of ^{61}V , ^{62}Cr , ^{64}Mn , and ^{65}Fe , which all had similar $B\rho$ values. Ions implanted in the DSSD were identified on an event-by-event basis from the relationship between the energy deposited in PIN2 (Si, 1041 μm) and the time of flight for an ion to travel from a thin plastic timing detector at the image of the A1900 to the PIN2 detector located approximately 40 cm upstream of the implantation site. A detailed study of the particle identification can be found in Ref. [42], which included event-by-event momentum corrections and confirmed that each particle group corresponded to only a single isotope.

B. Decay-implant correlation

Due to the presence of multiple isotopes in the beam, it is essential to identify each ion event-by-event and correlate its implantation with the corresponding β decay. This is done

by associating specific decay events (energy deposited in SuN and a valid high gain energy signal in a single pixel of the DSSD) in the data stream with specific implantation events (no energy signal in SuN and a low-gain energy signal above threshold in the same DSSD pixel). The implantation event that is nearest in time preceding a decay event and recorded in the same pixel should be paired. Unfortunately, it is possible that the nearest preceding implant to a particular decay is not the decay parent but is actually a random correlation. While it is impossible to exactly untangle such effects on an event-by-event basis when there are multiple isotopes in the beam, the various spectra (see Sec. III D) can be corrected for random misidentified events. The rate and spectral shape of the correction to each individual spectrum can be determined by looking for the nearest following implant for each decay event. Because this violates causality it will never be the correct parent for the decay but spectra from these pairs will have the same properties as would spectra from incorrect correlations done with the correct time ordering.

To analyze the full β -delayed γ decay of an isotope of interest, decays are correlated in both directions and the resulting random spectra (where the implant occurs after the decay) are subtracted from the real spectra (where the implant precedes the decay but where not every correlation is correct). The random spectra are normalized so that events with long time differences are of equal intensity in both. In this analysis those were events with time differences between decay and implant between nine and ten seconds. To further minimize random events in the real spectra, implantation events that registered within one second of each other were rejected.

While this method works well for reducing the background in γ -ray measurements, it is not well suited to the time spectra from which the parent half-life can be determined. Because the method always pairs a decay with the nearest implant there is a bias toward short decay times that distorts the exponential shape of the decay-time spectrum. Another slightly different method of correlation, here called “unbiased correlation,” was implemented for the half-life analysis. This method of correlation involves correlating each β -decay event with all the implantation events within the correlation time window on a pixel-by-pixel basis. As is the case with the biased correlation, the time period prior to the β decay will contain the correct implant for correlation (along with random implants), while the time period following decay will only contain random correlations. The unbiased correlation method ensures that one of the correlated pairs is the correct real correlation (implant before decay) and it ensures that the random background is not time dependent. While this does result in a large background, it avoids distortion of the shape of the time spectrum, making it ideal for half-life analysis. The unbiased correlation method is not suitable for γ analysis because of the much higher rate of incorrect correlation (lower signal to noise ratio).

C. Half-life analysis

There are previous measurements of the half-life of the ground state of ^{64}Mn tabulated in the ENSDF database provided by the National Nuclear Data Center (NNDC). The evaluated value reported there is 90(4) ms [43]. Additionally,

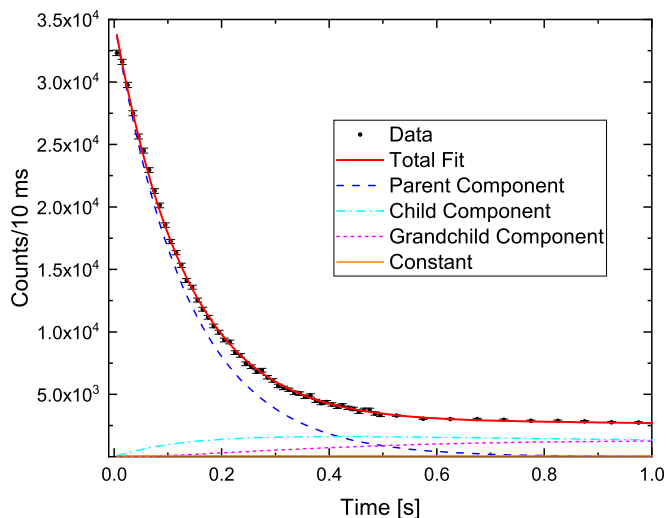


FIG. 1. Distribution of the measured time between implant and decay after subtracting the random events. Decay events were associated with implant events with the unbiased correlation method (see text). The data were fit with a function derived from the Bateman equations [44], to properly account the buildup and decay of the child nucleus. The fits results give a half-life of 90.5(20) ms for ^{64}Mn .

the ^{64}Fe child and ^{64}Co grandchild half-lives are reported as 2.0(4) s and 0.30(3) s, respectively [43].

Here, a half-life was extracted based on the time between implant and subsequent β decay based on the unbiased correlation method. Because the unbiased method matches an observed β decay with the observed implant events (within a 10 s window) decays of the implanted ^{64}Mn parent, as well as decays of the ^{64}Fe child and ^{64}Co grandchild, are recorded. The time spectrum for random correlations (decay before implant) was subtracted from the properly ordered times before fitting. Random correlations were scaled so as to eliminate any negative counts at long times when subtracting them from the real correlations. The resulting spectrum and fit are shown in Fig. 1 for the first 1 s. The fit function was based on Bateman parent-child-grandchild functions [44] and a constant background. The results of this fit (and the statistical uncertainties from the fit) give a parent half-life of 90.5(20) ms, in good agreement with the literature values.

D. γ analysis

In this work, the I_β is determined from three basic spectra: the TAS spectrum itself, the sum-of-segments spectrum, and the multiplicity spectrum (number of SuN segments registering energy) [21,22,26,40,45–48]. Due to the high efficiency of SuN, both intrinsic and geometrical, most of the γ rays from a decay cascade can be detected, which gives the TAS spectrum. This spectrum provides insight into the populated level in the child nucleus. Since SuN is made up of eight optically isolated NaI(Tl) crystals, the energy of each γ ray in a cascade can also be determined. This is the sum-of-segments spectrum, and it gives insight into the individual γ rays from the de-excitation of a given level in the child nucleus. In conjunction with the sum-of-segments spectrum, the multiplicity spectrum

provides information on how many γ rays were emitted in a given decay path. These three spectra can all be modeled with GEANT4 [49], which takes into account physical complexities such as geometrical effects, actual detection efficiency, energy resolution, Compton scattering, multiple γ rays being detected in the same segment, and higher energy β particles reaching the scintillator, as well as the details of the decay cascade from a particular excited state.

In order to reduce the impact from the child-nucleus decay, a time gate rejecting events after one parent half-life [90.5(20) ms, this work] was applied. Calculations with the Bateman equations indicated that due to the much longer child half-life [2.0(4) s, NNDC] this reduces the child nucleus contribution to a negligible level ($\approx 1.7\%$).

To further increase the quality of data, γ events were required to fall within a 640 ns time window after the detection of a β particle.

E. $I_\beta(E)$ extraction

The β -decay intensity function is found by simulating the response of each SuN detector segment for all possible decay paths to create the three analysis spectra (TAS, sum-of-segments, and multiplicity spectra). In this process the same restrictions applied to experimental data are imposed upon the simulated events. A global fit to minimize χ^2 is then performed by varying the contribution of each child level to the spectra. In order to create these simulations, GEANT4 requires information about each child level and the γ -ray branching ratios. Discrete level input information (energy, branching ratios, and J^π) was extracted from NNDC. The discrete levels of the child nucleus are only known up to a certain critical energy, which was chosen as 3316.8 keV. This child level energy was chosen because fits with the last β -allowed level listed in RIPL3 and ENSDF (4226.8(5) keV [43]) did not reproduce the data as well. Thus, between the critical energy and the $Q(\beta^-)$ value (11.981(6) MeV [43]), nonoverlapping pseudolevels were created to represent the continuum of levels. This process was performed with RAINIER [50]. RAINIER takes input parameters such as the low-lying discrete level scheme, nuclear level density parameters, spin dependence, etc. and simulates randomly determined cascades. Input parameters for RAINIER were taken from NNDC, while the nuclear level density was described using the constant temperature model [51]. It should be noted that small changes in these input parameters result in variations within the 10% systematic uncertainty of the detector response [16]. The pseudolevel energy spacing was chosen based on the resolution of SuN in the respective energy region.

^{64}Fe has a neutron separation energy (S_n) of 7.405(7) MeV [43], which is well below the $Q(\beta^-)$ value. Pseudolevels between S_n and $Q(\beta^-)$ were created to account for the possibility of β -delayed neutron decay (β^-n). In order to simulate levels that underwent β^-n decay, RAINIER determined the energy level in the range of the desired energy such that the level was allowed based on spin and parity. Based on the observed γ -ray energies and selection rules, it was assumed the β^-n decay only fed the ground state and the 356 keV state in

^{63}Fe . GEANT4 modeled the interactions of the neutrons with the detector apparatus.

One additional discrete level was simulated with RAINIER at 2225 keV. This level was included to account for a peak in the TAS spectrum that was not explained by any listed levels or nuclei in the decay path. The level energy was chosen by performing multiple fits with varying level energies in the region of the unexplained peak. RAINIER determined the de-excitation path based on the known level scheme below 2225 keV. The veracity of this level was established by confirming the presence of characteristic γ rays from the level scheme in the sum-of-segments spectrum when gated on the unexplained peak in the TAS spectrum. (No strong feeding from the 2225 keV level to the ground state or any other level except the 746.6 keV level was observed.)

The characteristic spectra for each of the possible decay paths were created. In order to increase sensitivity to certain energy regions, nine more spectra were created with unique gates. Sum-of-segments and multiplicity were each gated on four separate regions of the TAS spectrum. Sum-of-segments was also gated on a γ -ray multiplicity of 1. The 12 spectra for each child-level's decay path were then used as basis states in a least-squares fitting function in which the coefficients for each basis state were varied to minimize χ^2 . An initial fit was performed in order to determine the relative intensities of states that underwent β^-n decay. Each β^-n state was then fixed to the resultant relative intensity and the sum was normalized to 1.56(6)% [52] based on a measurement of the β^-n strength for this system using the NERO detector [53]. The actual value from our fit was 1.37(14)% but the more precise NERO value was adopted. An older measurement of this probability was reported with a value of 2.7(6)% [54,55]. Then all the coefficients were then normalized to sum to 100% to give the I_β values. The best fit is given in Fig. 2 and compared to data and random correlations.

IV. RESULTS

A. $I_\beta(E)$

The individual $I_\beta(E)$ values extracted from the fitting process are presented in Table I. The $I_\beta(E)$ values are summed to form the cumulative $I_\beta(E)$ distribution, which is plotted in Fig. 3. In Fig. 3 one can see a strong ground-state-to-ground-state transition strength. Even while there is no γ ray emitted for decay to the child ground state, the associated β particles are detected in SuN with a shape extending to the maximum energy seen in Fig. 2, allowing for an accurate determination of this strength. As described above, the model space of simulated decays contained pseudo levels to account for γ decays from higher energies. The fit also included a second set of pseudolevels with energies greater than the neutron separation energy that populated either the ground or first excited state in ^{63}Fe . The contribution of these levels could be extracted because the TAS and sum-of-segments spectra showed γ rays from ^{63}Fe and neutron capture energy in SuN itself. It should be noted that above S_n , starting with levels at 7.5 MeV, the fitting algorithm only attributed strength to levels that decayed via β^-n emission.

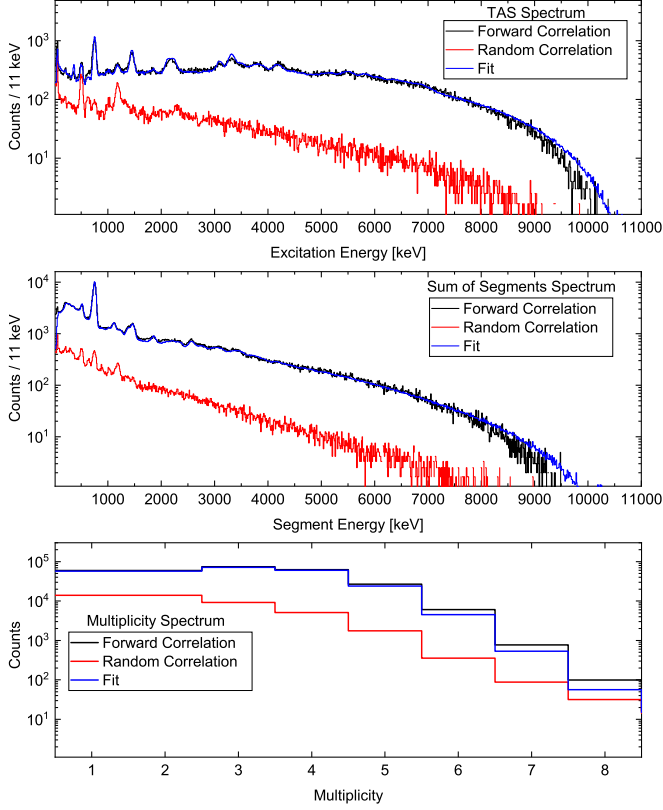


FIG. 2. The best least-squares fits of the TAS, sum-of-segments, and γ -ray multiplicity spectra for ^{64}Mn . The blue curve is the sum of the individual simulated spectra for the various levels, scaled according to intensity, added to the random correlation.

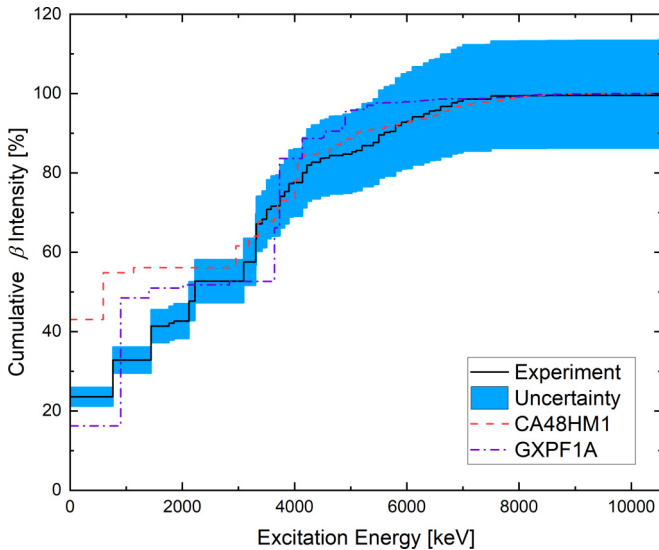


FIG. 3. Experimentally determined cumulative $I_\beta(E)$ for the decay of ^{64}Mn to ^{64}Fe . Results shown are from β -delayed γ decay of ^{64}Mn (below 7500 keV) and β -delayed neutron decay (above 7500 keV). Shell model calculations with CA48MH1 and GXPF1A effective interaction Hamiltonians are shown by the red dashed line and violet dot-dashed line, respectively. The shaded region shows uncertainties determined by least-squares fit.

TABLE I. $I_\beta(E)$ for the decay of ^{64}Mn to ^{64}Fe . All intensity values below $5 \times 10^{-5}\%$ are omitted. Pseudolevels start with 3420 keV (the tabulated energy is the center of the pseudolevel) and levels starting at 7.5 MeV decay only by neutron emission (β^- delayed neutrons). The lower-limit of uncertainties (combined systematic and statistical) has been adjusted to prevent nonphysical negative β feedings. The level at 2225 keV has not been observed in previous experiments, but was identified in this work.

Energy (keV)	Intensity (%)	Error (\pm)	Energy (keV)	Intensity (%)	Error (\pm)
0.0	23.5	2.4	4620	0.57	0.13
746.6	9.2	0.9	4860	0.29	0.14
1443.7	8.6	0.9	5020	0.60	0.15
1763	0.75	0.11	5100	0.36	0.13
1853.2	0.53	0.11	5200	1.19	0.19
2116.7	5.0	0.5	5400	0.82	0.18
2225	5.0	0.5	5500	1.9	0.3
3093.4	4.8	0.5	5600	0.67	0.21
3306.8	5.6	0.6	5700	0.22	0.18
3317.0	4.0	0.4	5800	1.51	0.27
3420	1.11	0.19	5900	0.77	0.23
3500	2.52	0.29	6000	0.28	0.17
3580	0.79	0.15	6100	1.12	0.20
3660	0.15	0.08	6300	0.74	0.16
3740	2.34	0.28	6400	0.68	0.15
3820	1.21	0.20	6500	0.21	0.07
3900	2.00	0.26	6600	0.97	0.16
3980	0.24	0.08	6800	0.96	0.18
4140	2.5	0.3	6900	0.38	0.16
4220	1.90	0.27	7000	0.52	0.10
4300	0.78	0.17	7200	0.024	$^{+0.027}_{-0.024}$
4460	0.96	0.18	≥ 7500 (β^-n)	1.56	0.06
4540	0.14	$^{+0.15}_{-0.14}$			

B. $B(\text{GT})$

The Gamow-Teller distribution was calculated from the $I_\beta(E)$ with the equation

$$B(\text{GT}) = \frac{I_\beta(E)}{f(Q_\beta - E)T_{1/2}} \times K \left(\frac{g_V}{g_A} \right)^2 \quad (1)$$

where $f(Q_\beta - E)$ is the Fermi integral, K is 6143.6(17) s [56], and g_A/g_V is $-1.2694(28)$ [57]. The measured value for $T_{1/2}$ was used in Eq. (1). The cumulative $B(\text{GT})$ compared to shell model calculations are shown in Fig. 4.

C. Theory

The β -decay properties of ^{64}Mn were calculated using the NUSHELLX@MSU code [58] with the effective interaction Hamiltonians GXPF1A [59,60] in the pf model space and CA48MH1 [61] in the CA48PN model space. In the CA48PN model space the protons occupy the single-particle orbits $\pi(0f_{7/2}^{(6-t)}, 0f_{5/2}^t, 1p_{3/2}^t, 1p_{1/2}^t)$ with $t = 0-2$ and the neutrons occupy the single particle orbits $\nu(0f_{5/2}^{(2-6)}, 1p_{3/2}^{(2-4)}, 1p_{1/2}^{(0-2)}, 0g_{9/2}^{(0-4)})$, where the same occupation numbers were used as in [62]. A reduction factor, R , equal to 0.55 was used for the Gamow-Teller rates in the pf model

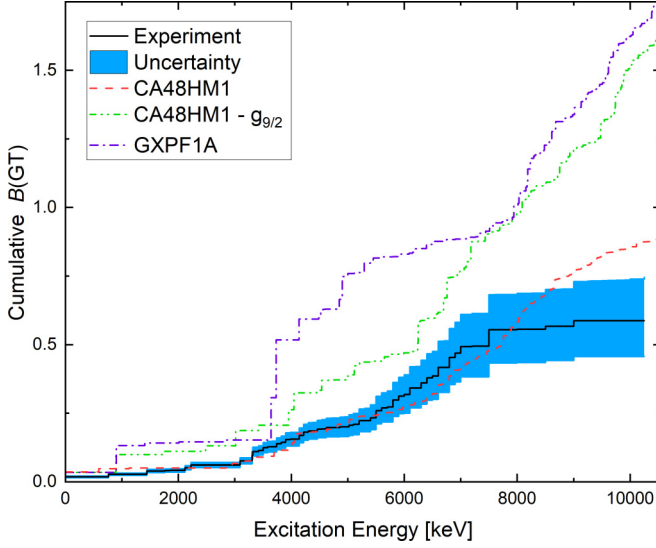


FIG. 4. $B(\text{GT})$ distribution calculated with experimentally determined $I_\beta(E)$ for the decay of ^{64}Mn to ^{64}Fe . Shell model calculations with CA48MH1 and GXPF1A effective interaction Hamiltonians are shown by the red dashed line and violet dot-dashed line, respectively. The green double-dot-dashed line shows shell model calculations with CA48MH1 effective interaction when the $g_{9/2}$ orbit is not occupied. The shaded region represents uncertainties propagated from least-squares fit.

space [63] and equal to 0.50 in the CA48PN model space. The experimental half-life of the parent state is 90(4) ms [43] [84.8(5) ms from this measurement], and the half-lives calculated with the GXPF1A and the CA48MH1 effective interactions are 34 ms and 87 ms, respectively. The shell model low energy spectra of the parent nucleus, ^{64}Mn , and the child nucleus, ^{64}Fe , are summarized in Tables II and III. The CA48MH1 effective interaction correctly predicts that the spin and parity of the ground state of ^{64}Mn is 1^+ , while the GXPF1A effective interaction predicts that the 1^+ is the third excited state. The β -decay shell model calculations were run assuming the 1^+ state to be the ground state for both effective interactions, given the close proximity in energy of the yrast 1^+ state predicted by the GXPF1A effective interaction to the ground state.

The experimental ground state β decay of ^{64}Mn feeds mainly the ground state in ^{64}Fe with an intensity of approximately 20% and the first two excited states with an intensity of approximately 8% each. The shell model β -decay intensity of ^{64}Mn with the CA48MH1 effective interaction closely follows the experimental values for excitation energies above

TABLE II. ^{64}Mn low energy levels (MeV).

Expt. spectrum	GXPF1A	CA48MH1
1^+ 0.000	0^+ 0.000	1^+ 0.000
$2^{(-)}$ 0.040	2^+ 0.040	2^+ 0.050
4^+ 0.175	5^+ 0.248	3^+ 0.243
2^+ 0.186	1^+ 0.273	4^+ 0.331

TABLE III. ^{64}Fe low energy levels (MeV).

Expt. spectrum	GXPF1A	CA48MH1
0^+ 0.000	0^+ 0.000	0^+ 0.000
2^+ 0.746	2^+ 0.901	2^+ 0.589
2^+ 1.444	2^+ 1.404	2^+ 1.132

3 MeV. However, it predicts a higher ground state feeding with an intensity of 43%, followed by the feeding of the first two excited states with an intensity of 12% and 1.3%, respectively. The GXPF1A effective interaction predicts that the β -decay branching to the first excited state in ^{64}Fe is the most strong, with an intensity of 32%, while the branching to the ground state in ^{64}Fe is 16%. The experimental β decay of ^{64}Mn is dominated by a few strong feedings towards the low energy region of ^{64}Fe , followed by a fragmented β -decay intensity above 3 MeV. This behavior is better reproduced by the CA48MH1 effective interaction which produces feedings of strong intensities below 3 MeV followed by a fragmented β -decay intensity above 3 MeV. The GXPF1A effective interaction predicts β -decay feedings with strong intensities up to about 5 MeV before the β -decay intensity becomes fragmented.

In Fig. 4, the $B(\text{GT})$ distribution predicted by the CA48MH1 effective interaction is in excellent agreement with the experimental data, while the GXPF1A calculations overestimate the cumulative $B(\text{GT})$. For both effective interactions the distribution of the Gamow-Teller strength is dominated by the spin-flip $\nu f_{5/2} \rightarrow \pi f_{7/2}$ decay, as the last neutrons in ^{64}Mn occupy the $f_{5/2}$ orbit. The dominance of the spin-flip $\nu f_{5/2} \rightarrow \pi f_{7/2}$ decay explains why the CA48MH1 cumulative Gamow-Teller strength distribution is significantly lower compared to the GXPF1A distribution. With the introduction of the $g_{9/2}$ orbit with the CA48MH1 effective interaction,

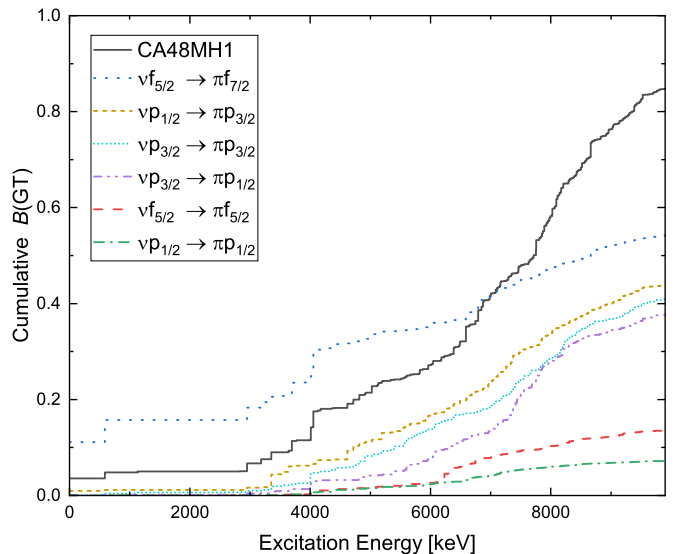


FIG. 5. Shell model calculations of the $B(\text{GT})$ distribution with CA48MH1 effective interaction against the contribution of a single decay to the $B(\text{GT})$ distribution with the same effective interaction.

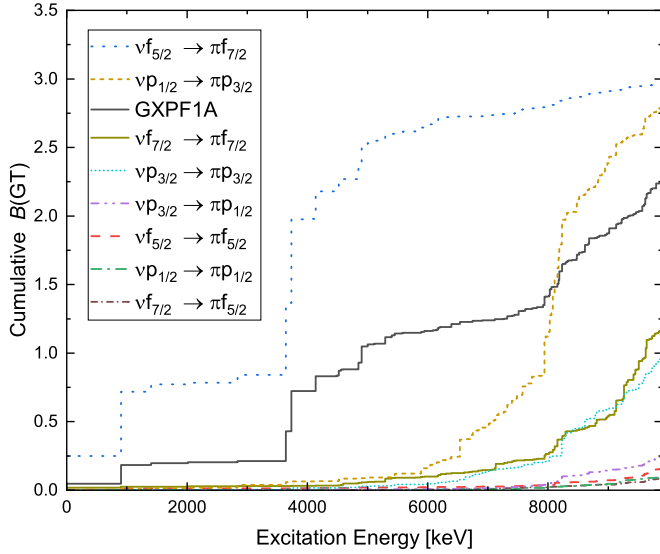


FIG. 6. Shell model calculations of the $B(GT)$ distribution with GXPF1A effective interaction against the contribution of a single decay to the $B(GT)$ distribution with the same effective interaction.

the $\nu f_{5/2}$ occupancy of the first 1^+ energy level of ^{64}Mn drops from 5.02 in the GXPF1A effective interaction, to 3.19 in the CA48MH1 effective interaction, as neutrons occupy the $g_{9/2}$ orbit. Figure 4 also shows the $B(GT)$ distribution of the CA48MH1 effective interaction when the neutron $g_{9/2}$ orbit is not occupied. The latter $B(GT)$ distribution follows closely the GXPF1A $B(GT)$. The $\nu g_{9/2} \rightarrow \pi g_{9/2}$ decay cannot be calculated with the CA48MH1 effective interaction, but it should not contribute to the Gamow-Teller strength below 7 MeV of energy. The steep increase of the GXPF1A cumulative Gamow-Teller strength above 8 MeV is mainly due to the contribution of the spin-flip $\nu p_{1/2} \rightarrow \pi p_{3/2}$ decay with the $\nu p_{3/2} \rightarrow \pi p_{3/2}$ and $\nu f_{7/2} \rightarrow \pi f_{7/2}$ decays having a smaller contribution. The increase of the CA48MH1 cumulative Gamow-Teller strength above 7 MeV can be attributed to the $\nu p_{1/2} \rightarrow \pi p_{3/2}$, $\nu p_{3/2} \rightarrow \pi p_{3/2}$, and $\nu p_{3/2} \rightarrow \pi p_{1/2}$ decays. The contribution of each decay for each effective interaction is seen in Figs. 5 and 6.

The inclusion of the $g_{9/2}$ neutron intruder orbit with the CA48MH1 effective interaction does not impact the low-energy spectrum of ^{64}Fe or the low energy β -decay strength; indeed the GXPF1A and CA48MH1 effective interactions predict similar low energy β -decay strengths. The role of the $g_{9/2}$ neutron intruder orbit becomes important above 3 MeV, in agreement with previous studies [8], rendering the spectrum of ^{64}Fe richer in energy levels at higher energy compared to

the GXPF1A spectrum. The ground state β decay of ^{64}Mn feeds these high energy levels with small intensities, giving the fragmented β -decay intensity observed in the experiment. The observed agreement between experiment and theory only when the $g_{9/2}$ orbital is included in the calculations once again confirms the transitional nature of ^{64}Fe moving towards the $N = 40$ island of inversion.

V. CONCLUSIONS

The present work reported the first total absorption measurement of the β -decay intensity and strength distributions for the decay of ^{64}Mn into ^{64}Fe . The experimental results were compared to shell model calculations with two interactions. Shell model calculations with the CA48MH1 Hamiltonian apportion too much strength to the ground-state-to-ground-state transition, but otherwise exhibit overall good agreement in shape. The GXPF1A calculations produce a similar ground-state-to-ground-state transition strength, but otherwise ascribe the majority of the strength to two levels at ≈ 1 MeV and ≈ 4 MeV. Our results highlight the need to include the $\nu g_{9/2}$ orbital in the description of ^{64}Fe , in agreement with previous studies.

ACKNOWLEDGMENTS

The authors acknowledge support of the operations staff at the National Superconducting Cyclotron Laboratory. The work was supported by the National Science Foundation under Grants No. PHY-1913554, No. PHY-2209429, No. PHY-1430152, No. PHY-1613188, and No. PHY-1848177 (CAREER). This material is based upon work supported by the Department of Energy/National Nuclear Security Administration through the Nuclear Science and Security Consortium under Award No. DE-NA0003180. This material is based upon work supported by the U.S. Department of Energy, Office of Science, Office of Nuclear Physics, under Contract No. DE-AC02-06CH11357. This work was also supported by the U.S. Department of Energy Office of Science under Grants No. DE-FG02-88ER40387 and No. DE-SC0019042 and the U.S. National Nuclear Security Administration through Grant No. DE-NA0003909. This work was performed under the auspices of the U.S. Department of Energy by Lawrence Livermore National Laboratory under Contract No. DE-AC52-07NA27344. S.L. was supported by the Laboratory Directed Research and Development Program at Pacific Northwest National Laboratory operated by Battelle for the U.S. Department of Energy. The authors would like to thank B. A. Brown for helpful discussions.

[1] E. K. Warburton, J. A. Becker, and B. A. Brown, *Phys. Rev. C* **41**, 1147 (1990).
 [2] S. M. Lenzi, F. Nowacki, A. Poves, and K. Sieja, *Phys. Rev. C* **82**, 054301 (2010).
 [3] A. Gade, *Physics* **3**, 1226 (2021).
 [4] A. Gade and S. N. Liddick, *J. Phys. G: Nucl. Part. Phys.* **43**, 024001 (2016).

[5] M. Hannawald *et al.*, *Phys. Rev. Lett.* **82**, 1391 (1999).
 [6] M. Hannawald, *Kernspectroskopie an N = 40 und N = 82 Nukliden*, Ph.D. thesis, Johannes Gutenberg University Mainz, 2000 (unpublished).
 [7] H. Heylen *et al.*, *Phys. Rev. C* **92**, 044311 (2015).
 [8] N. Hoteling, W. B. Walters, R. V. F. Janssens, R. Broda, M. P. Carpenter, B. Fornal, A. A. Hecht, M. Hjorth-Jensen,

- W. Królás, T. Lauritsen, T. Pawłat, D. Seweryniak, X. Wang, A. Wöhr, J. Wrzesiński, and S. Zhu, *Phys. Rev. C* **74**, 064313 (2006).
- [9] S. Lunardi, S. M. Lenzi, F. Della Vedova, E. Farnea, A. Gadea, N. Mărginean, D. Bazzacco, S. Beghini, P. G. Bizzeti, A. M. Bizzeti-Sona, D. Bucurescu, L. Corradi, A. N. Deacon, G. de Angelis, E. Fioretto, S. J. Freeman, M. Ionescu-Bujor, A. Iordachescu, P. Mason, D. Mengoni *et al.*, *Phys. Rev. C* **76**, 034303 (2007).
- [10] J. Jungvall, A. Görgen, A. Obertelli, W. Korten, E. Clément, G. de France, A. Bürger, J.-P. Delaroche, A. Dewald, A. Gadea, L. Gaudefroy, M. Girod, M. Hackstein, J. Libert, D. Mengoni, F. Nowacki, T. Pissulla, A. Poves, F. Recchia, M. Rejmund *et al.*, *Phys. Rev. C* **81**, 061301(R) (2010).
- [11] W. Rother, A. Dewald, H. Iwasaki, S. M. Lenzi, K. Starosta, D. Bazin, T. Baugher, B. A. Brown, H. L. Crawford, C. Fransen, A. Gade, T. N. Ginter, T. Glasmacher, G. F. Grinyer, M. Hackstein, G. Ilie, J. Jolie, S. McDaniel, D. Miller, P. Petkov *et al.*, *Phys. Rev. Lett.* **106**, 022502 (2011).
- [12] M. P. Carpenter, R. V. F. Janssens, and S. Zhu, *Phys. Rev. C* **87**, 041305(R) (2013).
- [13] Y. Fujita, B. Rubio, and W. Gelletly, *Prog. Part. Nucl. Phys.* **66**, 549 (2011).
- [14] J. Hardy, L. Carraz, B. Jonson, and P. Hansen, *Phys. Lett. B* **71**, 307 (1977).
- [15] M. Karny, K. Rykaczewski, A. Fijakowska, B. Rasco, M. Woliska-Cichocka, R. Grzywacz, K. Goetz, D. Miller, and E. Zganjar, *Nucl. Instrum. Methods Phys. Res. Sect. A* **836**, 83 (2016).
- [16] A. Simon, S. J. Quinn, A. Spyrou, A. Battaglia, I. Beskin, A. Best, B. Bucher, M. Couder, P. A. DeYoung, X. Fang, J. Görres, A. Kontos, Q. Li, S. N. Liddick, A. Long, S. Lyons, K. Padmanabhan, J. Peace, A. Roberts, D. Robertson *et al.*, *Nucl. Instrum. Methods Phys. Res. Sect. A* **703**, 16 (2013).
- [17] C. Reingold, O. Olivas-Gomez, A. Simon, J. Arroyo, M. Chamberlain, J. Wurzer, A. Spyrou, F. Naqvi, A. Dombos, A. Palmisano *et al.*, *Eur. Phys. J. A* **55**, 77 (2019).
- [18] O. Olivas-Gomez, A. Simon, D. Robertson, A. Dombos, F. Strieder, T. Kadlecsek, M. Hanhardt, R. Kelmar, M. Couder, J. Görres *et al.*, *Eur. Phys. J. A* **58**, 57 (2022).
- [19] B. Rubio, W. Gelletly, A. Algora, E. Nacher, and J. L. Tain, *J. Phys. G: Nucl. Part. Phys.* **44**, 084004 (2017).
- [20] V. Guadilla, J. Tain, A. Algora, J. Agramunt, J. Äystö, J. Briz, A. Cucoanes, T. Eronen, M. Estienne, M. Fallot, L. Fraile, E. Ganioglu, W. Gelletly, D. Gorelov, J. Hakala, A. Jokinen, D. Jordan, A. Kankainen, V. Kolhinen, J. Koponen *et al.*, *Nucl. Instrum. Methods Phys. Res. Sect. A* **910**, 79 (2018).
- [21] A. C. Dombos, Ph.D. thesis, Michigan State University, 2018 (unpublished).
- [22] J. Gombas, P. A. DeYoung, A. Spyrou, A. C. Dombos, A. Algora, T. Baumann, B. Crider, J. Engel, T. Ginter, E. Kwan, S. N. Liddick, S. Lyons, F. Naqvi, E. M. Ney, J. Pereira, C. Prokop, W. Ong, S. Quinn, D. P. Scriven, A. Simon, and C. Sumithrarachchi, *Phys. Rev. C* **103**, 035803 (2021).
- [23] S. N. Liddick, A. Spyrou, B. P. Crider, F. Naqvi, A. C. Larsen, M. Guttormsen, M. Mumpower, R. Surman, G. Perdikakis, D. L. Bleuel, A. Couture, L. Crespo Campo, A. C. Dombos, R. Lewis, S. Mosby, S. Nikas, C. J. Prokop, T. Renstrom, B. Rubio, S. Siem, and S. J. Quinn, *Phys. Rev. Lett.* **116**, 242502 (2016).
- [24] A. C. Dombos, D. Robertson, A. Simon, T. Kadlecsek, M. Hanhardt, J. Görres, M. Couder, R. Kelmar, O. Olivas-Gomez, E. Stech, F. Strieder, and M. Wiescher, *Phys. Rev. Lett.* **128**, 162701 (2022).
- [25] E. Nacher, A. Algora, B. Rubio, J. L. Tain, D. Cano-Ott, S. Courtin, P. Dessagne, F. Maréchal, C. Miehe, E. Poirier, M. J. G. Borge, D. Escrig, A. Jungclaus, P. Sarriguren, O. Tengblad, W. Gelletly, L. M. Fraile, and G. LeScornet, *Phys. Rev. Lett.* **92**, 232501 (2004).
- [26] A. Spyrou, S. N. Liddick, F. Naqvi, B. P. Crider, A. C. Dombos, D. L. Bleuel, B. A. Brown, A. Couture, L. Crespo Campo, M. Guttormsen, A. C. Larsen, R. Lewis, P. Möller, S. Mosby, M. R. Mumpower, G. Perdikakis, C. J. Prokop, T. Renström, S. Siem, S. J. Quinn, and S. Valenta, *Phys. Rev. Lett.* **117**, 142701 (2016).
- [27] A. Algora, D. Jordan, J. L. Tain, B. Rubio, J. Agramunt, A. B. Perez-Cerdan, F. Molina, L. Caballero, E. Nacher, A. Krasznahorkay, M. D. Hunyadi, J. Gulyás, A. Vitéz, M. Csatlós, L. Csige, J. Äystö, H. Penttilä, I. D. Moore, T. Eronen, A. Jokinen *et al.*, *Phys. Rev. Lett.* **105**, 202501 (2010).
- [28] A. Fijakowska, M. Karny, K. P. Rykaczewski, B. C. Rasco, R. Grzywacz, C. J. Gross, M. Woliska-Cichocka, K. C. Goetz, D. W. Stracener, W. Bielewski, R. Goans, J. H. Hamilton, J. W. Johnson, C. Jost, M. Madurga, K. Miernik, D. Miller, S. W. Padgett, S. V. Paulauskas, A. V. Ramayya, and E. F. Zganjar, *Phys. Rev. Lett.* **119**, 052503 (2017).
- [29] M. Estienne, M. Fallot, A. Algora, J. Briz-Monago, V. M. Bui, S. Cormon, W. Gelletly, L. Giot, V. Guadilla, D. Jordan, L. LeMeur, A. Porta, S. Rice, B. Rubio, J. L. Tain, E. Valencia, and A. A. Zakari-Issoufou, *Phys. Rev. Lett.* **123**, 022502 (2019).
- [30] C. Horowitz *et al.*, *J. Phys. G* **46**, 083001 (2019).
- [31] Z. Meisel, A. Deibel, L. Keek, P. Shternin, and J. Elfritz, *J. Phys. G: Nucl. Part. Phys.* **45**, 093001 (2018).
- [32] P. Möller, B. Pfeiffer, and K. L. Kratz, *Phys. Rev. C* **67**, 055802 (2003).
- [33] T. Marketin, L. Huther, and G. Martínez-Pinedo, *Phys. Rev. C* **93**, 025805 (2016).
- [34] E. M. Ney, J. Engel, T. Li, and N. Schunck, *Phys. Rev. C* **102**, 034326 (2020).
- [35] B. D. Metzger, A. Arcones, E. Quataert, and G. Martínez-Pinedo, *Mon. Not. R. Astron. Soc.* **402**, 2771 (2010).
- [36] H. Klion, A. Tchekhovskoy, D. Kasen, A. Kathirgamaraju, E. Quataert, and R. Fernández, *Mon. Not. R. Astron. Soc.* **510**, 2968 (2021).
- [37] D. J. Morrissey, B. M. Sherrill, M. Steiner, A. Stolz, and I. Wiedenhoever, *Nucl. Instrum. Methods Phys. Res., Sect. B* **204**, 90 (2003).
- [38] A. Stolz, T. Baumann, T. Ginter, D. Morrissey, M. Portillo, B. Sherrill, M. Steiner, and J. Stetson, *Nucl. Instrum. Methods Phys. Res. Sect. B* **241**, 858 (2005).
- [39] A. C. Dombos, A. Spyrou, F. Naqvi, S. J. Quinn, S. N. Liddick, A. Algora, T. Baumann, J. Brett, B. P. Crider, P. A. DeYoung, T. Ginter, J. Gombas, E. Kwan, S. Lyons, W.-J. Ong, A. Palmisano, J. Pereira, C. J. Prokop, D. P. Scriven, A. Simon, M. K. Smith, and C. S. Sumithrarachchi, *Phys. Rev. C* **99**, 015802 (2019).
- [40] A. C. Dombos, A. Spyrou, F. Naqvi, S. J. Quinn, S. N. Liddick, A. Algora, T. Baumann, J. Brett, B. P. Crider, P. A. DeYoung, T. Ginter, J. Gombas, S. Lyons, T. Marketin, P. Möller, W.-J. Ong, A. Palmisano, J. Pereira, C. J. Prokop, P. Sarriguren, D. P. Scriven, A. Simon, M. K. Smith, and S. Valenta, *Phys. Rev. C* **103**, 025810 (2021).

- [41] W.-J. Ong, E. F. Brown, J. Browne, S. Ahn, K. Childers, B. P. Crider, A. C. Dombos, S. S. Gupta, G. W. Hitt, C. Langer, R. Lewis, S. N. Liddick, S. Lyons, Z. Meisel, P. Möller, F. Montes, F. Naqvi, J. Pereira, C. Prokop, D. Richman, H. Schatz, K. Schmidt, and A. Spyrou, *Phys. Rev. Lett.* **125**, 262701 (2020).
- [42] W.-J. Ong, Ph.D. thesis, Michigan State University, 2018 (unpublished).
- [43] B. Singh and J. Chen, *Nucl. Data Sheets* **178**, 41 (2021).
- [44] H. Bateman, *Proc. Cambridge Philos. Soc.* **15**, 423 (1910).
- [45] F. Naqvi, S. Karampagia, A. Spyrou, S. Liddick, A. Dombos, D. Bleuel, B. Brown, L. Crespo Campo, A. Couture, B. Crider, T. Ginter, M. Guttormsen, A. Larsen, R. Lewis, P. Möller, S. Mosby, G. Perdikakis, C. Prokop, T. Renstrøm, and S. Siem, *Nucl. Phys. A* **1018**, 122359 (2022).
- [46] C. F. Persch, P. A. DeYoung, S. Lyons, A. Spyrou, S. N. Liddick, F. Naqvi, B. P. Crider, A. C. Dombos, J. Gombas, D. L. Bleuel, B. A. Brown, A. Couture, L. Crespo Campo, J. Engel, M. Guttormsen, A. C. Larsen, R. Lewis, S. Karampagia, S. Mosby, E. M. Ney *et al.*, *Phys. Rev. C* **103**, 055808 (2021).
- [47] S. Lyons, A. Spyrou, S. N. Liddick, F. Naqvi, B. P. Crider, A. C. Dombos, D. L. Bleuel, B. A. Brown, A. Couture, L. C. Campo, J. Engel, M. Guttormsen, A. C. Larsen, R. Lewis, P. Möller, S. Mosby, M. R. Mumpower, E. M. Ney, A. Palmisano, G. Perdikakis *et al.*, *Phys. Rev. C* **100**, 025806 (2019).
- [48] A. C. Dombos, D.-L. Fang, A. Spyrou, S. J. Quinn, A. Simon, B. A. Brown, K. Cooper, A. E. Gehring, S. N. Liddick, D. J. Morrissey, F. Naqvi, C. S. Sumithrarachchi, and R. G. T. Zegers, *Phys. Rev. C* **93**, 064317 (2016).
- [49] S. Agostinelli, J. Allison, K. Amako, J. Apostolakis, H. Araujo, P. Arce, M. Asai, D. Axen, S. Banerjee, G. Barrand, F. Behner, L. Bellagamba, J. Boudreau, L. Broglia, A. Brunengo, H. Burkhardt, S. Chauvie, J. Chuma, R. Chytráček, G. Cooperman *et al.*, *Nucl. Instrum. Methods Phys. Res. Sect. A* **506**, 250 (2003).
- [50] L. E. Kirsch and L. A. Bernstein, *Nucl. Instrum. Methods Phys. Res. Sect. A* **892**, 30 (2018).
- [51] T. von Egidy and D. Bucurescu, *Phys. Rev. C* **80**, 054310 (2009).
- [52] W. J. Ong (private communication).
- [53] J. Pereira, P. Hosmer, G. Lorusso, P. Santi, A. Couture, J. Daly, M. Del Santo, T. Elliot, J. Görres, C. Herlitzius, K.-L. Kratz, L. Lamm, H. Lee, F. Montes, M. Ouellette, E. Pellegrini, P. Reeder, H. Schatz, F. Schertz, L. Schnorrenberger *et al.*, *Nucl. Instrum. Methods Phys. Res. Sect. A* **618**, 275 (2010).
- [54] D. Pauwels, D. Radulov, W. B. Walters, I. G. Darby, H. De Witte, J. Diriken, D. V. Fedorov, V. N. Fedosseev, L. M. Fraile, M. Huyse, U. Köster, B. A. Marsh, L. Popescu, M. D. Seliverstov, A. M. Sjödin, P. Van den Bergh, J. Van de Walle, P. Van Duppen, M. Venhart, and K. Wimmer, *Phys. Rev. C* **86**, 064318 (2012).
- [55] M. Birch, B. Singh, I. Dillmann, D. Abriola, T. Johnson, E. McCutchan, and A. Sonzogni, *Nucl. Data Sheets* **128**, 131 (2015).
- [56] J. C. Hardy and I. S. Towner, *Nucl. Phys. News* **16**, 11 (2006).
- [57] K. Nakamura and P. D. Group, *J. Phys. G* **37**, 075021 (2010).
- [58] B. A. Brown and W. D. M. Rae, *Nucl. Data Sheets* **120**, 115 (2014).
- [59] M. Honma, T. Otsuka, B. A. Brown, and T. Mizusaki, *Phys. Rev. C* **69**, 034335 (2004).
- [60] M. Honma, T. Otsuka, B. Brown, and T. Mizusaki, *Eur. Phys. J. A* **25**, 499 (2005).
- [61] M. Hjorth-Jensen, T. T. Kuo, and E. Osnes, *Phys. Rep.* **261**, 125 (1995).
- [62] R. Schwengner, S. Frauendorf, and B. A. Brown, *Phys. Rev. Lett.* **118**, 092502 (2017).
- [63] G. Martínez-Pinedo, A. Poves, E. Caurier, and A. P. Zuker, *Phys. Rev. C* **53**, R2602 (1996).